The Astrophysical Journal, 936:30 (14pp), 2022 September 1 https://doi.org/10.3847/1538-4357/ac86d5
© 2022. The Author(s). Published by the American Astronomical Society.
OPEN ACCESS

Exomoons as Sources of White Dwarf Pollution

Isabella L. Trierweiler[1], Alexandra E. Doyle[2], Carl Melis[3], Kevin J. Walsh[4], and Edward D. Young[2]
[1] Department of Earth, Planetary, and Space Sciences, UCLA, Department of Physics and Astronomy, University of California, Los Angeles, CA 90095-1562, USA; itrierweiler@g.ucla.edu
[2] Department of Earth, Planetary, and Space Sciences University of California, Los Angeles Los Angeles, CA 90095, USA; eyoung@epss.ucla.edu
[3] Center for Astrophysics and Space Sciences, University of California, San Diego, CA 92093-0424, USA; cmelis@ucsd.edu
[4] Southwest Research Institute 1050 Walnut Street, Suite 400, Boulder, CO 80302, USA
Received 2022 May 13; revised 2022 August 2; accepted 2022 August 2; published 2022 August 29

Abstract

Polluted white dwarfs (WDs) offer a unique way to study the bulk compositions of exoplanetary material, but it is not always clear if this material originates from comets, asteroids, moons, or planets. We combine *N*-body simulations with an analytical model to assess the prevalence of extrasolar moons as WD polluters. Using a sample of observed polluted WDs, we find that the extrapolated parent body masses of the polluters are often more consistent with those of many solar system moons, rather than solar-like asteroids. We provide a framework for estimating the fraction of WDs currently undergoing observable moon accretion based on results from simulated WD planetary and moon systems. Focusing on a three-planet WD system of super-Earth to Neptune-mass bodies, we find that we could expect about one percent of such systems to be currently undergoing moon accretions as opposed to asteroid accretion.

Unified Astronomy Thesaurus concepts: White dwarf stars (1799); Planetary dynamics (2173)

1. Introduction

White dwarfs (WDs) are the end-states of medium-mass stars ($M_* \lesssim 8M_\odot$), and their high gravity leads to rapid sinking of any elements heavier than helium. This sinking occurs on timescales of days to millions of years (Koester 2009; Blouin et al. 2018), and generally leaves the spectra of WDs devoid of metal features. Nevertheless, over 1000 WDs have been observed to be "polluted" with heavy elements (Coutu et al. 2019), with estimates that up to half of all WDs are polluted (Koester et al. 2014). The source of the pollution is believed to be the remains of rocky parent bodies, which survived the post-main-sequence evolution of the host star. Surviving planets can scatter these bodies onto highly eccentric orbits, such that the objects approach the WD and are tidally disrupted and subsequently accreted by the star (e.g., Debes & Sigurdsson 2002; Jura 2003).

The majority of WD polluters appear rocky (Swan et al. 2019; Doyle et al. 2020) and a few appear icy (Farihi et al. 2013; Hoskin et al. 2020). Many accreted bodies are chondritic in composition, and based on this and their apparent masses, it has been often assumed that these parent bodies were small rocky bodies analogous to the asteroids, or Kuiper Belt objects (Xu et al. 2017), in the solar system. Here we attempt to quantify the fraction of polluting bodies that are exomoons rather than asteroids based on the parent body masses required for observed WDs and numerical simulations of the frequency of each population's accretion. We are motivated by the recent discovery of beryllium in a polluted WD (Klein et al. 2021) and the interpretation that the observed large excess in Be relative to other rock-forming elements is a tell-tale indicator that the parent body accreted by the WD was an icy moon. In this interpretation, the excess Be is the result of irradiation of the icy moon in the radiation belt of its host giant planet (Doyle et al. 2021). Payne et al. (2016) and Payne et al. (2017) showed that moons can be liberated by close encounters between planets and that liberated moons could be accreted by a WD. Here we examine this proposal in greater detail using a statistical analysis and *N*-body simulations of the liberation and accretion of moons.

The probability of observing a moon versus an asteroid depends on the frequency and duration of the respective accretion events relative to the detectable amount of pollution on a typical WD. Based on occurrence rates of dust around A-type stars, debris belts are expected to be ubiquitous among polluted WD progenitors (Melis 2016). Accordingly, assuming that any planetary systems with moons available for accretion would also have a debris belt available, the probability of observing a moon versus an asteroid accretion in a given WD system is

$$\frac{P_{\text{moon accretion}}}{P_{\text{asteroid accretion}}} = \frac{T_{\text{moons}}}{T_{\text{asteroids}}}, \quad (1)$$

where T is the fraction of time that the associated population provides observable pollution. Because we are interested in cumulative times, T is dependent on the accretion rate of each population ($T = T$(accretion rate)).

Because asteroids are expected to accrete much more frequently than moons due to their sheer number, $P_{\text{moonaccretion}}/P_{\text{asteroidaccretion}}$ will depend on whether the accumulation of successive asteroid accretions is sufficient to sustain high masses of WD pollution, compared to the single accretion events of relatively larger-mass moons.

In this paper we estimate the parameters of Equation (1) for a system of three super-Earth to Neptune-mass planets. A number of planetary architectures are capable of becoming unstable and aiding to feed material to the WD (e.g., Veras & Gänsicke 2015; Stephan et al. 2017; Maldonado et al. 2022); however, we focus on this particular system because existing

Original content from this work may be used under the terms of the Creative Commons Attribution 4.0 licence. Any further distribution of this work must maintain attribution to the author(s) and the title of the work, journal citation and DOI.

studies of asteroid (debris) belts in this architecture provide a baseline against which to compare moon accretions.

Our paper is organized around Equation (1). In Section 2 we introduce an analytical model for masses of polluting elements in the WD convection zone, which we apply to all accretion events throughout this work. We show that this model implies that observed polluted WDs require masses much larger than one would expect for typical asteroid belt objects, emphasizing the need to understand moon accretions. In Section 3 we use observations of polluted WDs to put limits on the levels of pollution required for the accretor to be detectable. Section 4 finds $T_{\rm asteroids}$, the cumulative timescale of detectability of asteroid pollution, using extrapolated asteroid accretion frequencies from previous studies. We present the results from our own *N*-body simulations for moon accretions in Section 4.2, and find $T_{\rm moons}$. Finally, we summarize all quantities and discuss the implications of Equation (1) in Section 5.

2. Analytical Model for Convection Zone Masses

To determine the duration and pollution levels associated with an accretion event, we make use of the model by Jura et al. (2009) for the buildup of accreted material in a WD atmosphere. Throughout this work, we will refer to the model as J09. The model describes the time-dependent mass of the polluter currently observable in the convection zone of a WD as a function of polluting parent body mass, element settling times through the WD atmosphere, and the duration of the accretion event. The model assumes the accretion disk, and therefore accretion rate, decay exponentially as one might expect from dissipative forces that depend on mass. Under this assumption, the mass of element Z that is observed to be in the convection zone of the WD at the time of observation t after the start of the accretion event, $M_{CV}(Z, t)$, is:

$$M_{\rm CV}(Z,t) = \frac{M_{\rm PB}(Z)\tau_{\rm set}(Z)}{\tau_{\rm disk} - \tau_{\rm set}(Z)}\left(e^{-t/\tau_{\rm disk}} - e^{-t/\tau_{\rm set}(Z)}\right), \qquad (2)$$

where $M_{\rm PB}(Z)$ is the mass of element Z in the parent body, $\tau_{set}(Z)$ is the e-folding settling time of element Z, and $\tau_{\rm disk}$ is the characteristic lifetime of the accretion disk.

The observable pollution mass $M_{\rm CV}(Z, t)$ in J09 depends on the settling timescale, which in turn depends on the properties of the host star. Therefore, variations in WD temperature and composition have significant impacts on the maximum accumulations of pollution in the WD atmosphere and the timescales during which pollution levels are sufficiently high to be observable. In Figure 1 we show the pollution masses for a representative element and parent body in a DA (top) and a DB (bottom) WD in order to illustrate these differences. Defined spectroscopically, DAs have atmospheres dominated by hydrogen, while those of DB WDs are helium-dominated. While WD classifications extend well beyond these two categories, for simplicity we will restrict our discussion to these two broad categories, using the terms DA and DB to mean hydrogen and helium-dominated in what follows. The primary difference between the two types of WDs in the present context is that DAs generally have settling timescales for the heavy elements of days to thousands of years, while the DBs have settling timescales of 10^5–10^6 yr for these elements. Additionally, because hot DAs will have minimal, if any, convection zones, we consider $M_{\rm CV}$ to more generally represent the mass of observable pollution in the WD atmosphere for these cases.

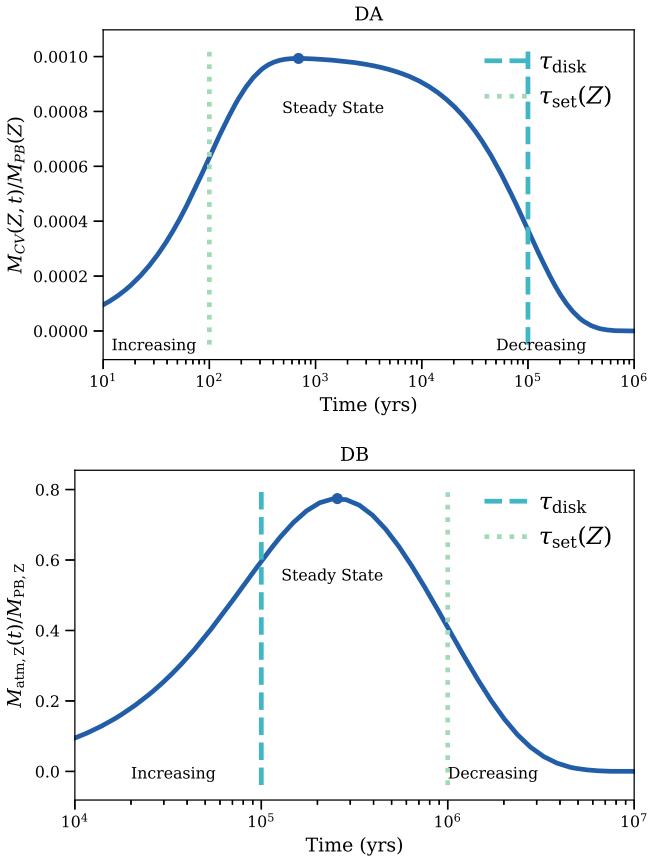

Figure 1. Examples of the fraction of parent body masses of a particular element that are predicted to be in the convection zone of a WD as a function of time, according to the J09 model (Equation (2)). We assume an accretion disk lifetime of 10^5 yr and settling times of 10^2 yr for the DA (top) and 10^6 yr for the DB (bottom). Note the three phases of accretion: increasing, steady state, and decreasing. While analogous phases occur both for the DA and DB, the timescales defining the boundaries of each phase are swapped due to the longer DB settling times.

The maximum heavy element mass in the convection zone for each WD type occurs where settling times are approached. In other words, the maximum is the amount of accreted material that can build up in the atmosphere before sinking exerts an influence on the abundances. In the example to follow, we assume a settling time of 10^2 yr for the DA and 10^6 yr for the DB. Both cases are assigned an accretion disk e-folding lifetime of 10^5 yr.

In Figure 1, we show the fraction of the parent body mass that is currently observable in the convection zone as a function of time since the start of accretion, for an exemplary heavy element. Both cases illustrate the three phases of pollution: while accretion is ongoing and before settling begins, the mass of the element builds up in the atmosphere (increasing phase). When the settling and accretion rates equalize (the blue point in Figure 1), the mass stays relatively constant (steady state). Once settling dominates as accretion wanes, the mass of the pollution decreases rapidly (decreasing phase). Note that, in this model, the majority of a single accretion event is in a decreasing phase.

Because settling in the DBs begins after the majority of the parent body has been accreted onto the WD, DBs can exhibit much larger fractions of the polluting metals than DAs, for the

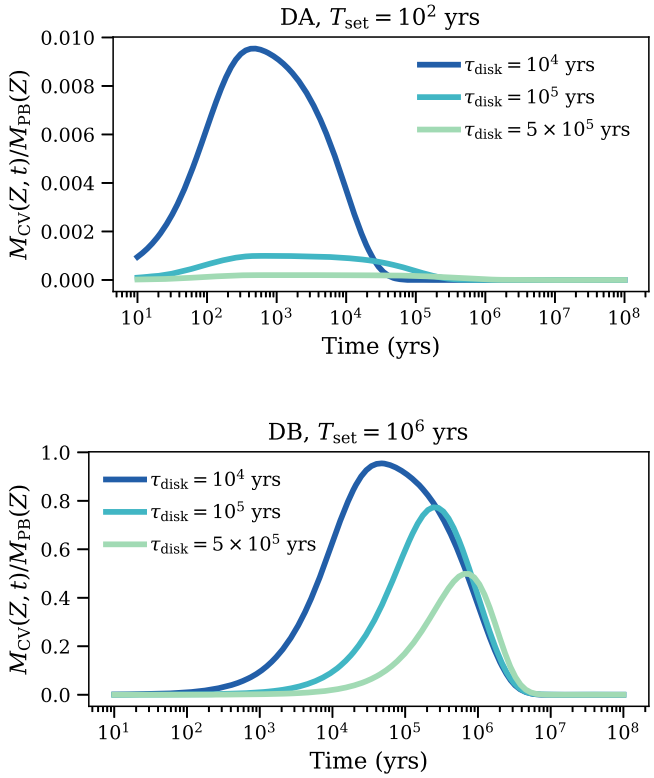

Figure 2. Fraction of parent body mass for a typical rock-forming element in the convection zone of a WD as a function of time, for three different accretion disk lifetimes. The DA pollution curves decrease by nearly a factor of 10 with increasing disk times, while the DB curves decrease less significantly. The peaks of both curves shift to later times as the disk accretion time increases, reflecting changes in the time where steady state between accretion and settling is achieved.

same parent body mass. The DA steady-state phase occurs earlier and therefore at relatively higher settling and accretion rates than the DB phase, and the two DA rates conspire to cause very small fractions of the parent body to be observable at any given time.

Estimates for τ_{disk} generally range from 10^4 to 10^6 yr (e.g., Girven et al. 2012). In Figure 2 we show how varying the disk timescale changes the pollution curves for the theoretical DA and DB stars shown in Figure 1. In particular, note that the maximum of the DA pollution decreases much more rapidly with increasing disk lifetimes than in the case of DBs.

We employ J09 in two ways. First, we estimate the parent body masses responsible for observed pollution in a sample of 21 WDs and compare these masses with the distribution of asteroid and moon masses in our own solar system (Section 2.1). Second, we use the model in conjunction with the average masses of asteroids and moons to determine the timescales of observability for both populations (Section 3).

2.1. Steady-state Parent Body Masses

In order to calculate parent body masses for polluted WDs, observed pollution masses ($M_{CV}(Z)$) and settling times were collected from the references in Table 1. The total masses of heavy elements in each WDs are shown in Figure 3. For an assumed disk timescale, we then solve Equation (2) for the parent body mass at a range of possible elapsed accretion times for each observed element in the WD. This gives an expression for the mass of element Z in the parent body for an assumed elapsed accretion time t_{elapse} and an observed metal mass of M_{CV} (Z):

$$M_{PB}(Z, t_{elapse}) = \frac{M_{CV}(Z)(\tau_{disk} - \tau_{set})}{\tau_{set}(e^{-t_{elapse}/\tau_{disk}} - e^{-t_{elapse}/\tau_{set}})}. \quad (3)$$

Note that we change the time variable to t_{elapse} to emphasize the difference in the meaning of time between Equations (2) and (3). Equation (2) solved for the variation in polluting element mass with time since accretion for a single parent body mass. Equation (3) instead takes an observed heavy metal mass and provides a range of parent body solutions that depend on the time at which one assumes the observation was taken. To obtain the total parent body mass solution, we sum over all observed elements at a given elapsed accretion time, such that $M_{PB}(t_{elapse}) = \sum M_{PB}(Z, t_{elapse})$.

As an example, Figure 4 shows the application of Equation (3) to the DA G149-28, and DB WD 2207+121. The vertical lines show the settling times for each element associated with each WD and the assumed disk lifetimes of 10^5 yr. Note that the shape of the parent body solution is roughly the inverse of the pollution mass curve, reaching a minimum during the steady-state phase of accretion, when the pollution mass is at a maximum. Equation (3) shows that the steady-state point, $dM_{PB}(Z, t_{elapse})/dt_{elapse} = 0$, coinciding with the minimum estimate for the parent body mass, will occur at time:

$$t_{min} = \frac{\tau_{disk}\tau_{set}}{\tau_{disk} - \tau_{set}} \ln\left(\frac{\tau_{disk}}{\tau_{set}}\right). \quad (4)$$

In practice, when summing over multiple elements as in Figure 4, each element would reach the steady-state point at slightly different times, due to the variations in settling times. Nonetheless, as long as the range of settling times is well above or below the disk lifetime, solving for elemental abundances at the time corresponding to steady state will give a minimum estimate for the total parent body mass. Thus, for the remainder of this work, one can think of the "minimum parent body mass" to be analogous to the "parent body solution assuming steady state." Note that this does not necessarily mean we are assuming all WDs are in steady state, but rather that any other phase of accretion would require a more-massive parent body than the steady-state solution to explain the observed metal pollution.

We calculate parent body masses for the WDs in Table 1 using the effective temperature and log g values reported in the references to obtain the WD convection zone masses and elemental settling times from the Montreal White Dwarf Database (MWDD; Dufour et al. 2017). We then derive $M_{CV}(Z)$ values from the relative abundances reported in the references, using the MWDD settling times and WD envelope mass fractions. For comparison, we also considered the models provided by Koester et al. (2020), which calculate settling times that include the lack of convection zones in hot, hydrogen-dominated WDs. We find that the settling timescales derived in the Koester models are generally comparable to those reported by the MWDD, and therefore do not significantly change the resulting parent body masses.

Additionally, while we use all stellar parameters from the MWDD instead of those reported in each reference, we find that in most cases, the values are in agreement, to within a factor of a few.

Table 1
All White Dwarf Parameters Collected from References

White Dwarf	Type	$T_{\rm eff}$ (K)	log(g)	$T_{\rm cool}$ (Gyr)	M$_*$ ($M_\odot$)	log(q)	Disk[b]	Reference
NLTT 43806	DAZ	5830	8.00	2.4237	0.587	−6.661	N	Zuckerman et al. (2011)
G149-28	DAZ	8600	8.10	1.0683	0.657	−9.224	N	Zuckerman et al. (2011)
G29-38	DAZ	11820	8.40	0.7452	0.858	−12.61	Y	Xu et al. (2014)
GD 133	DAZ	12600	8.10	0.3960	0.667	−15.434	Y	Xu et al. (2014)
SDSS J1043+0855	DA	18330	8.05	0.1095	0.649	−16.645	Y	Melis & Dufour (2017)
WD 1226+110	DAZ	20900	8.15	0.0812	0.714	−16.663	Y	Gänsicke et al. (2012)
WD 1929+012	DAZ	21200	7.91	0.0388	0.578	−16.283	Y	Gänsicke et al. (2012)
WD 0446-255	DBAZ	10120	8.00	0.6355	0.581	−5.242	N	Swan et al. (2019)
GD 362	DB	10540	8.24	0.8098	0.732	−5.789	Y	Xu et al. (2013)
PG 1225-079	DBAZ	10800	8.00	0.5343	0.582	−5.235	Y	Xu et al. (2013)
WD 1350-162	DBAZ	11640	8.02	0.4484	0.596	−5.273	N	Swan et al. (2019)
WD 1232+563	DBZA	11787	8.30	0.6623	0.773	−5.924	N	Xu et al. (2019)
SDSS J0738+1835	DBZA	13950	8.40	0.495	0.842	−6.324	Y	Dufour et al. (2012)
HS 2253+8023	DBAZ	14400	8.40	0.4541	0.842	−6.408	N	Klein et al. (2011)
WD 2207+121	DBZ	14752	7.97	0.2046	0.572	−5.591	Y	Xu et al. (2019)
WD 1551+175	DBAZ	14756	8.02	0.2230	0.601	−5.691	Y	Xu et al. (2019)
WD 1145+017	DBZA	14500	8.11	0.2746	0.655	−5.819	Y	Fortin-Archambault et al. (2020)
GD 40	DBZA	15300	8.00	0.1912	0.591	−5.805	Y	Jura et al. (2012)
G241-6	DB	15300	8.00	0.1912	0.591	−5.805	N	Jura et al. (2012)
Ton 345	DB	19780	8.18	0.1097	0.706	−7.883	Y	Wilson et al. (2015)
WD 1536+520	DBA	20800	7.96	0.0491	0.578	−8.938	N	Farihi et al. (2016)

Notes. Any values not reported by the paper have been supplemented using the Montreal White Dwarf Database (Dufour et al. 2017). Throughout this work, we group WDs by their primary classification type (DA or DB only).
[a] q is the fraction of stellar mass in the stellar envelope. Note that the DA WDs have much smaller stellar envelopes.
[b] Debris disks indicated for WDs with detected infrared excesses.

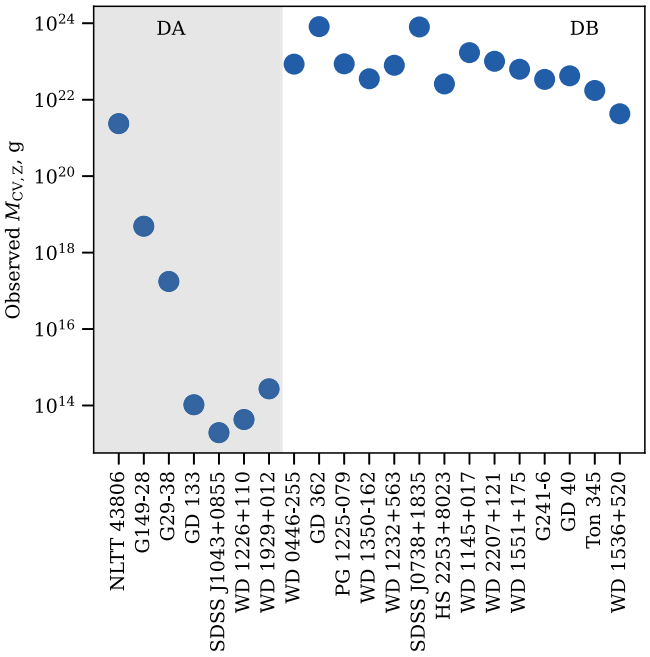

Figure 3. Total masses of heavy metals observed for the WDs in Table 1, sorted by type. The DAs tend to have lower observed masses of polluting elements compared to the DBs.

Minimum parent body solutions for the observed WDs are shown in Figure 5, for a range of disk timescales. Because of the marked dependence on disk lifetime (Figure 2), we expect variations in assumed disk lifetime to change the minimum parent body estimates for DAs much more than for DBs. This expectation is realized, as shown in Figure 5.

We find that the majority of parent body estimates for DB WDs are between roughly 10^{23}–10^{24} g regardless of the disk timescale chosen. DA estimates are generally orders of magnitude lower. A likely explanation for the DA/DB disparity is the effects of thermohaline mixing, which operates primarily on DAs (Bauer & Bildsten 2018). Accounting for thermohaline mixing effectively shortens settling timescales and requires DAs to have much higher accretion rates to explain observed pollution masses, which in turn increase their parent body masses (Bauer & Bildsten 2019). Nonetheless, both sets of parent body masses represent lower limits.

In Figure 6 we show how the distribution of calculated parent body masses (assuming a disk lifetime of 10^5 yr) compares to the distributions of moon masses in the solar system as well as to the approximate distribution of asteroid masses. Moon masses and radii are from the JPL Solar System Dynamics group[5]. We calculate the asteroid masses assuming the distribution of asteroid radii is $dN \propto r^{-3.5}dr$ (Dohnanyi 1969), and that all bodies have the same density of 3 g cm^{-3}. In reality, the majority of asteroids have lower densities ($\sim$2.5 g cm^{-3}), so we can consider the asteroid masses as upper limits. We assume that the range of asteroid diameters is 1–1000 km, corresponding with a range of masses of approximately 10^{15}–10^{24} g. The WD pollution parent body masses are generally far larger than those defined by the asteroid distribution. While the DA parent body masses and the majority of the DB masses reside in the range of the largest bodies in our asteroid belt, such as Ceres ($\sim10^{24}$ g) or Vesta ($\sim10^{23}$ g), they are well above the bulk of the asteroid mass distribution. From our sample, for a disk timescale of 10^5 yr, we consider a mean DA parent body to be $\sim10^{21}$ g and a mean DB to be $\sim10^{23}$ g. In our solar system, there are about 30 and

[5] https://ssd.jpl.nasa.gov/ (Giorgini et al. 1996) data taken 2021 August.

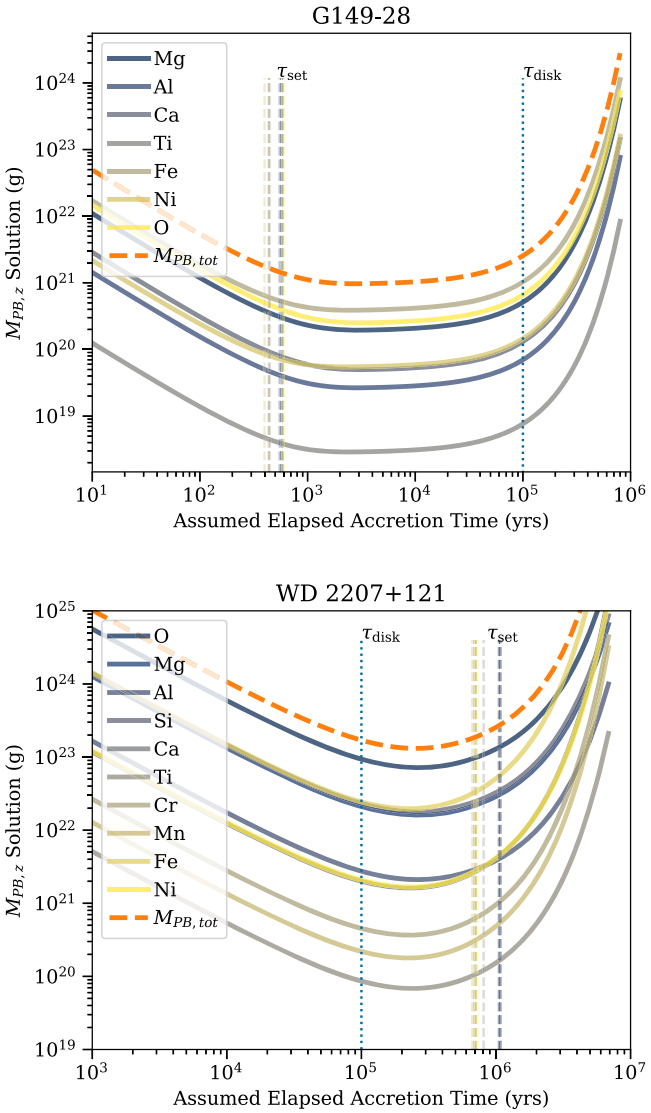

Figure 4. An example plot of the parent body mass calculated from Equation (3) as a function of assumed elapsed accretion time for the DA G149-28 (top) and DB WD 2207+121 (bottom). We assume an accretion disk lifetime of 10^5 yr (dotted line). Settling timescales for the DB are approximately 10^6 yr, those for the DA are ~400 yr, and both are marked in dashed lines for each element. The parent body solution derived from Equation (2) is plotted for each element, and the dashed orange line shows the sum of all parent body elements at each assumed elapsed accretion time.

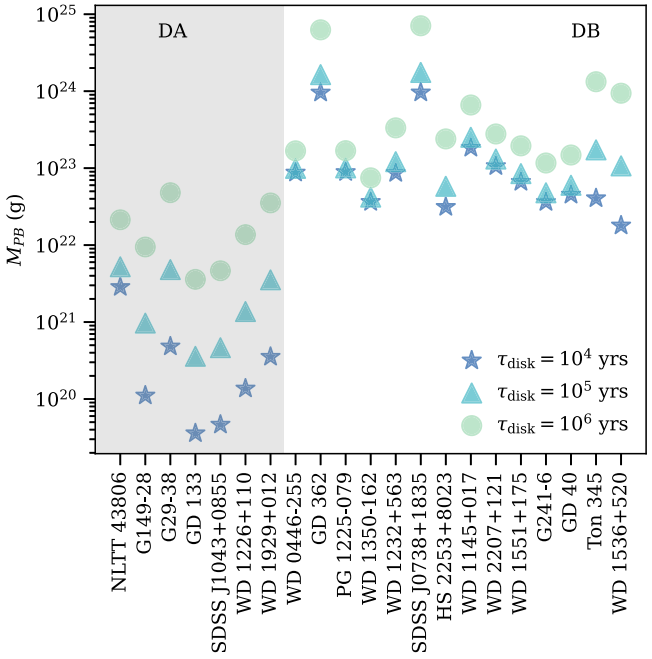

Figure 5. Parent body masses calculated assuming the WD is in steady state, with four different assumed accretion disk timescales. DA parent body solutions tend to vary more dramatically with disk timescale than the DBs. Most DB parent body mass solutions are close to ~10^{23}, and while the DA solutions are somewhat lower, the two begin to converge as disk timescales increase.

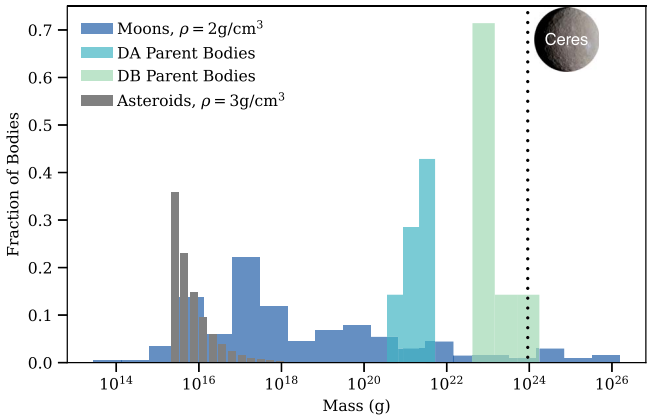

Figure 6. Fraction of bodies in each population with a given mass. Densities of 3 and 2 g cm^{-3} are assumed to calculate masses for asteroids and moons, respectively. The asteroid curve is derived from Dohnanyi (1969), and the moon data are from the JPL Solar System Dynamics group. The parent body masses are split into DA and DB populations and assume a disk lifetime of 10^5 yr. The DBs tend to have larger parent body mass solutions, though the masses for both the DAs and DBs are situated toward the tail end of asteroid masses and mid-to-high moon masses. For comparison, the mass of Ceres is indicated as the dotted line. Note that the parent body masses shown are lower limit solutions.

15 moons that fall above these DA and DB masses, respectively.

The large calculated parent body masses compared to minor solar system bodies implicate an observational bias. This may be partially due to the large masses required to detect pollution, which we outline in the next section.

3. Pollution Detection Limits

In Section 2.1, we showed that in the context of the J09 model, most observed WD pollution requires parent body masses consistent with the more-massive moons of the solar system, and the extremely rare most-massive asteroids. We now turn to observations to determine a lower limit of observable pollution in a WD atmosphere to place further constraints on the differences between moon and asteroid pollution.

Lower limits for observable masses of pollution in WD atmospheres are obtained from measurements of calcium masses in polluted WDs. We choose calcium because there is a large sample of observations for Ca available in the literature with which we can assess minimum masses. We collect Ca masses for DA WDs from the SPY Survey (Koester et al. 2005) and masses for the DBs from Zuckerman et al. (2010). We first approximate a line to the lowest calcium masses in the SPY survey to derive an expression for minimum mass as a function of effective temperature (Equation (5)). We then use the DB

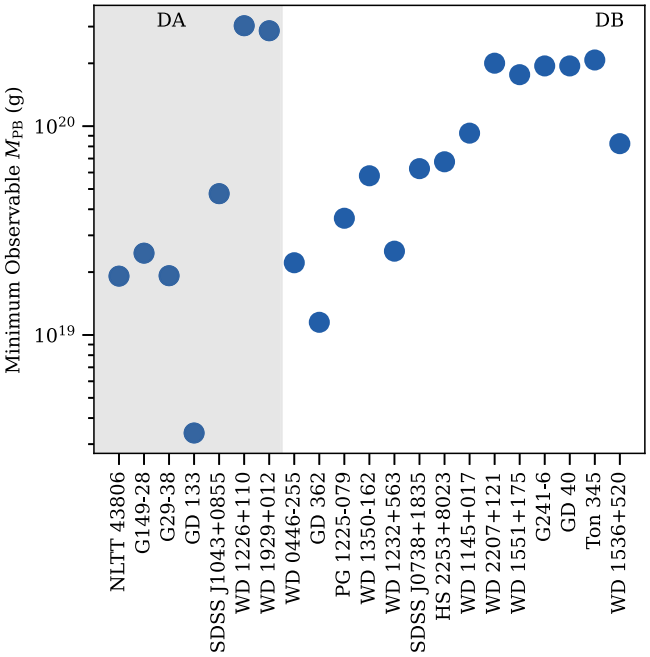

Figure 7. Calculated minimum detectable parent body masses associated with the detection limit for Ca, assuming chondritic parent body compositions. To obtain these masses, we solve the J09 model for the minimum mass of calcium in the parent body, assuming an $M_{\mathrm{CV,Ca}}$ according to Equation (5). We then calculate the minimum parent body mass solution by assuming chondritic composition, settling timescales from MWDD corresponding to the effective temperature of each WD, and a disk timescale of 10^5 yr.

data to renormalize the line for the DB WDs. Because the data are expressed by number relative to hydrogen/helium, the relation between the minimum masses and temperature is dependent on the mass of the convection zone (mass of hydrogen for DAs or helium for DBs). Our expressions for the minimum masses of Ca that are observable in the polluted WDs are

$$M_{\mathrm{min\ Ca,\ DA}} = 10^{\frac{4T_{\mathrm{eff}}(K)}{15000}-12.6} \times \frac{m_{\mathrm{Ca}}}{m_{\mathrm{H}}} \times M_{\mathrm{CV}}$$
$$M_{\mathrm{min\ Ca,\ DB}} = 10^{\frac{4T_{\mathrm{eff}}(K)}{15000}-14.2} \times \frac{m_{\mathrm{Ca}}}{m_{\mathrm{He}}} \times M_{\mathrm{CV}}, \quad (5)$$

where m_{Ca} is the mass of calcium, m_{H} is the mass of hydrogen, m_{He} is the mass of helium, and M_{CV} is the mass of the WD convection zone or WD atmosphere. As the atmospheres of DAs tend to be relatively small (see Table 1), their limits of detectable calcium mass are much lower than that of DBs.

Applying Equation (5) to the WDs in Table 1, we obtain the minimum detectable calcium mass in the observable layers for each WD. The DBs have detection limits of $\sim 10^{18}$ g Ca, while the DA limits extend to orders of magnitude lower. The lower limit for calcium detection in the DAs is consistent with their lower observed $M_{\mathrm{CV,Z}}$ values, as described above.

Taking the minimum observable calcium masses for each of the observed WDs, we now use the J09 model to calculate the parent body mass associated with each calcium mass limit. For each WD, we first apply the J09 model to the minimum detectable calcium mass to find the minimum mass of calcium in the parent body. We then calculate the total parent body mass by assuming chondritic composition ($\sim$1% calcium by mass), an accretion disk e-folding time of 10^5 yr, and settling times provided by the MWDD based on the effective temperature of each WD. Figure 7 shows the resulting parent body masses associated with the extrapolated minimum observed calcium mass for each WD in our sample. These bodies would provide just enough calcium pollution to be detected with current technology.

While the instantaneous minimum observable pollution masses derived from Equation (5) require much higher masses for the DBs, we find that DAs and DBs require similar overall parent body masses to produce observable pollution. This is due to the difference in fractions of the parent body that can build up in each type of atmosphere (Figure 1). Assuming each parent body is accreting as a single event, the resulting minimum parent body masses required for observable pollution for both types of WDs are generally larger than the mean for solar system asteroids, and closer to the masses of solar system moons, suggesting an observational bias against "typical" asteroids.

In the following sections, we will examine how moons and asteroids compare when we allow for continuous accretion of material. This approach is particularly necessary for asteroids, which are thought to reach accretion rates that require material from multiple objects to be present in the WD atmosphere at any one time. Going forward, we will adopt the instantaneous minimum observable mass limits of 5.3×10^{16} and 1.3×10^{20} g of total heavy elements for a typical DA ($T_{\mathrm{eff}} = 10{,}000$ K) and DB ($T_{\mathrm{eff}} = 14{,}000$ K), respectively. For single chondritic accretions, these limits correspond to minimum observable total parent body masses of 1.3×10^{19} g for the DA and 1.7×10^{20} g for the DB. Note that because DAs accumulate much smaller fractions of the parent body in their atmospheres at steady state, the minimum observable parent body masses for DAs and DBs are similar, despite orders of magnitude differences in their instantaneous limits.

4. Continuous Accretion Models for Asteroids and Moons

While describing the J09 model in Section 2, we considered the increasing, steady state, and decreasing phases for a single accreting body. However, it is possible that pollution in the WD atmosphere could be from multiple parent bodies. In particular, Mustill et al. (2018) found that asteroids can accrete onto WDs continuously for up to billions of years. To assess how much of the pollution from continuous accretion could fall within observable limits, we consider populations of potential polluters based on mass frequency distributions of asteroids and moons in the solar system as guides. We then use total accretion rates determined previously from *N*-body simulations to construct synthetic pollution curves by applying the J09 model (Equation (2)) to each event.

We currently restrict the comparison of moon and asteroid accretion to a three-planet system of super-Earths and Neptunes, a system that has previously been shown to result in high rates of asteroid accretion by Mustill et al. (2018). Additionally, we focus on the first 200 Myr past WD formation, the time frame in which asteroid pollution levels are expected to be at their maximum.

4.1. Asteroid Accretion

Mustill et al.'s (2018) simulations show that in the first few million years after WD formation, a debris belt can reach a peak accretion rate of $\sim 10^{-4} N_{\mathrm{AB}}\,\mathrm{Myr}^{-1}$, where N_{AB} is the number of asteroid belt objects. Because the 200 Myr time span

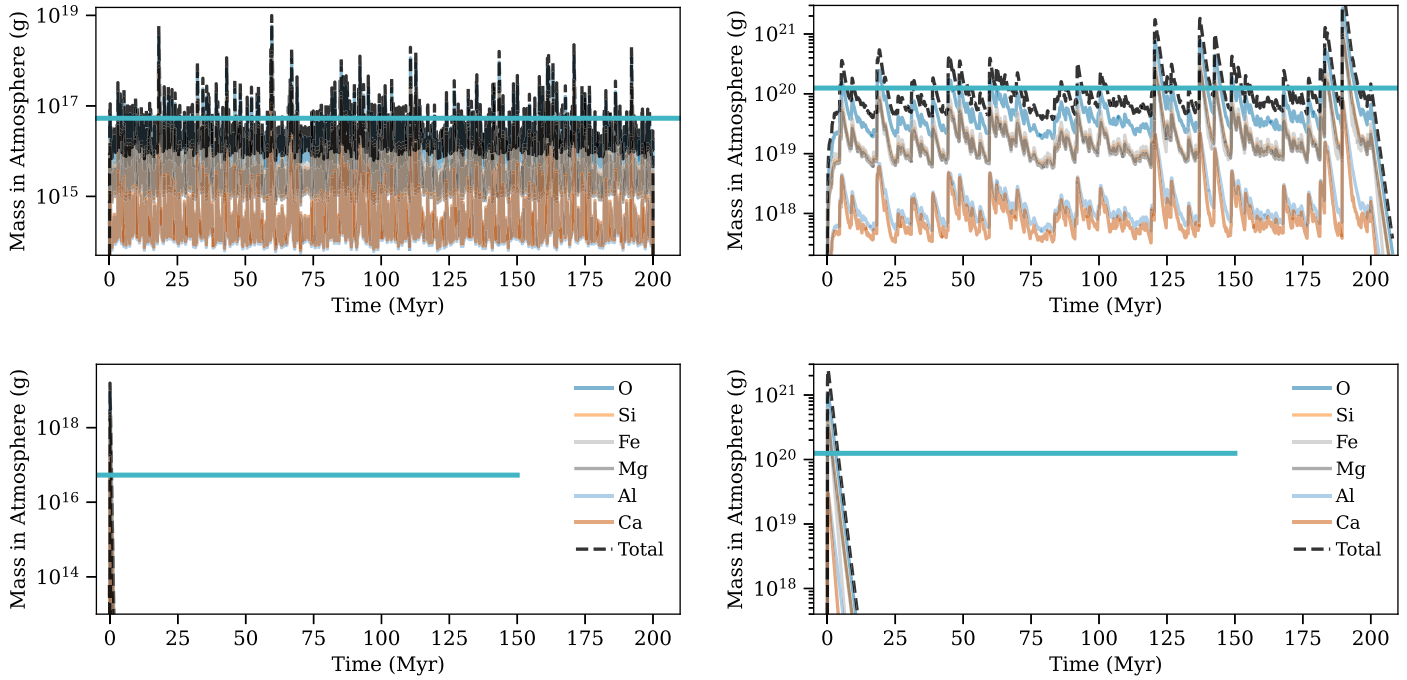

Figure 8. Synthetic pollution mass curve for an asteroid belt (top) and a single moon event (bottom) as a function of time post WD formation. The black dashed line shows the total mass of pollution in the convection zone, and the colored lines show the pollution mass per element. The horizontal line shows the minimum detectable mass of heavy elements. The left column shows accretion onto a DA WD, while the right shows pollution of a DB. Top row: continuous accretion of an asteroid-mass debris belt, based on the mean accretion rate of Mustill et al. (2018) and assuming the distribution of masses follows that of the solar system asteroid belt. Bottom row: accretion of a single moon of mass $\sim 10^{20}$ g onto a typical DA (left) and a moon of mass $\sim 10^{21}$ g onto a typical DB (right). These masses represent the median mass of the subset of solar system moons that satisfy the criteria for being liberated from their host planets and providing observable levels of metal pollution.

is relatively short compared to the full length of time considered in the Mustill simulations, we consider the accretion rate to be approximately constant in our calculations. We therefore use the accretion rate to constrain the total number of accretions that can occur within the 200 Myr period, and then pick the specific accretion event times randomly from a uniform distribution, such that each point in time is equally likely to be the start of an accretion event.

The masses of accreting bodies for each event are chosen at random, without replacement, from the distribution of masses representing the solar system asteroid belt. We assume a range of radii of 0.5–500 km and a total mass of the asteroid belt of 3×10^{24} g. Dohnanyi (1969) found the radius distribution for a collisionally generated debris belt to be $dN \propto r^{-3.5} dr$. Translating this distribution into masses, we have an asteroid mass range of $1.6 \times 10^{15} - 1.6 \times 10^{24}$ g and $dN \propto \rho^{5/6} m^{-11/6} dm$. The total mass of the belt is then $M_{\rm belt} \propto \int m dN$, which we constrain to be the mass of the asteroid belt. Assuming that all bodies are spherical, we obtain $M_{\rm belt} = A \int \rho \frac{4\pi}{3} r^3 r^{-3.5} dr$, where A is a constant, and ρ is the density of the asteroids. Assuming a constant density of 3 g cm^{-3} and our adopted radius range of 0.5–500 km, we find $dN = 1.7 \times 10^{19} r^{-3.5} dr$. This gives a total of about 12 million objects in the debris belt, of which about 2% are accreted in the full 200 Myr time period.

To sample this distribution, we split the range of asteroid masses into 12 bins, spaced logarithmically in mass, a choice that leaves one object in the Ceres-mass bin. We assign each object in the belt a mass bin according to the distribution described previously, again assuming a constant asteroid density of 3 g cm^{-3}. For each accretion event, we pick an object at random, identify its mass bin, and select a mass at random from the range of masses associated with that bin. We obtain masses of individual elements in the parent body by assuming chondritic composition, and then evolve these masses through the J09 model (Equation (2)) to track the total masses of polluting elements in the WD atmosphere. The number of bodies in the selected bin is then decreased by one.

The upper panels of Figure 8 show the results of this calculation assuming a disk e-folding time of 10^5 yr and settling times for a 10,000 K hydrogen-dominated WD and 14,000 K helium-dominated WD. Each peak in the figure corresponds with an accretion event, and is followed by a tail during which mass sinks out of the atmosphere. The colored curves show the mass of individual elements comprising the polluting debris in the convection zone as a function of time, and the black dashed curve shows the total mass of heavy elements in the convection zone. Note that because asteroid accretions are very frequent compared to the settling timescales, material from at least one body can be found in the mixing layer for the majority of the 200 Myr time interval.

In Section 3 we found that the minimum convection zone pollution mass that is observable is about 5.3×10^{16} g for a typical DA WD and 1.3×10^{20} g for a typical DB, as derived from observed calcium masses. The horizontal lines in Figure 8 show the detectability threshold, and any peaks in pollution that exceed these limits are considered detectable periods of accretion.

In both the DA and DB cases, a long-term mass of pollution is sustained in the atmosphere, with peaks when more-massive asteroids accrete. The sustained background pollution is generally not enough to exceed detection limits, but the more-massive asteroid accretions are observable. This suggests that while multiple debris belt objects may be contributing to observed pollution, it is likely that the majority of the observed

mass is due to a single, more-massive body. We find that asteroid accretions onto the DA can exceed the pollution detection limit for a total of ∼29 Myr, resulting in a cumulative fraction of observable time of $T_{\rm asteroids,DA} = 0.145$.

All else equal, pollution levels are higher for the DB case than the DA case as more mass can build up in the DB WD atmosphere due to slow settling times. Overall, in the DB simulation, the pollution is at an observable level for a total of ∼72 Myr out of the 200 Myr interval, such that $T_{\rm asteroids,DB} = 0.360$.

We note that in the asteroid accretion scenarios, the maximum masses of heavy elements that accumulate in the WD atmosphere are $\sim 5 \times 10^{16}$ g for the DA and $\sim 10^{20}$ g for the DB. From Figure 3, we see that the WDs in the observed sample have total masses of heavy metals that can exceed the maxima reached by our continuous asteroid accretion simulation by factors of up to $\sim 10^3$. In addition to the expected vicissitudes of extrasolar asteroid belt masses, we consider that the higher observed masses could be due to accretion of moons.

4.2. Moon Accretion Simulations

We carried out the same calculations for moons around WDs as we did for the asteroids in order to compare the expected detectability of accretion events for the two sources. For this purpose, we require an accretion rate for moons. This rate comes from the efficacy of liberating moons from host planets, and the accretion rate of the liberated moons onto the WD.

We simulate the separation of moons from their host planets during the stellar mass-loss event that produces the WDs in order to estimate $f_{\rm moons}$, the frequency of moon accretions by WDs. Because moon orbital periods require very short time steps for integration, we break down $f_{\rm moons}$ into two parts to accommodate computational limits. We define $f_{\rm moons}$ as $N_{\rm moons} \times f_{\rm accrete}$, where $N_{\rm moons}$ is the number of moons in the system that can be liberated from their host planets and are able to provide detectable levels of pollution on a WD, and $f_{\rm accrete}$ is how frequently a moon from this population reaches the WD.

We use the *N*-body code REBOUND (Rein & Liu 2012) to model three planets each with two moons. The IAS15 adaptive time step integrator (Rein & Spiegel 2015) allows time steps to be shortened or lengthened according to the occurrence of close encounters between particles. Due to computational limits, we set the smallest allowable time step to be 0.1 day. Following the approach described in Payne et al. (2017) for moon liberations, we start each simulation with a three-planet system (no moons) and integrate the planet orbits during stellar mass loss. The mass loss excites the planetary orbits, eventually leading to orbit crossings. We halt this portion of the simulation at the first orbit crossing, when the periapsis of any planet falls below the apoapsis of the adjacent interior planet, or, alternatively, when the apoapsis exceeds the periapsis of the adjacent exterior planet. At this point, we insert two test particle moons around each planet (six moons in total). The simulation is then resumed, including stellar mass loss if it is still ongoing.

During the moon and planet portion of the simulation, we consider a moon to be accreted by the WD if it passes within the Roche limit of the WD (∼0.005 au). However, we note that it is possible that bodies farther away than 0.005 au could still be accreted by the WD, for example through Alfvén wave drag (Zhang et al. 2021). Averaging the frequency of moon accretions across all simulation trials gives $f_{\rm accrete}$.

4.3. Initial Conditions for Moon Simulations

While Payne et al. (2016) use planetary architectures as simulated by Veras & Gänsicke (2015) and Veras et al. (2016) to assess moon accretion, we carry out our tests using the same three-planet system simulated by Mustill et al. (2018; Section 4) in order to compare our results for moon accretions to those of debris belt accretions.

Each of our simulations begins with three planets around a $3M_\odot$ main-sequence host star that evolves into a $0.75M_\odot$ WD. The planets have masses of 1.3, 30.6, and 7.8 $M_\oplus$ and initial semimajor axes of 10, 11.6, and 13.07 au, respectively, as prescribed by the Mustill simulations. We focus on this particular set of planets as they resulted in the largest fractions of asteroids engulfed by the WD in the Mustill study. We choose random initial inclinations in the range [0°,1°], initial eccentricities of zero, and random values between 0° and 360° for all other orbital angles.

Stellar mass loss is incorporated by updating the stellar mass according to the analytical formulae for single-star evolution by Hurley et al. (2000). This code calculates stellar properties over 1 Gyr. For simplicity, each of our simulations begins at the start of stellar mass loss such that WD formation occurs ∼100 Myr after the start of the simulation.

For the three-planet systems, the first orbit crossing usually occurs before the end of the stellar mass-loss event. Because mass loss speeds up significantly toward the end of the 100 Myr interval, the stellar mass is usually still close to $\sim 3M_\odot$, and the semimajor axes of the planets have generally not increased dramatically, when the simulation is paused for moon insertion.

We follow the prescription for moon insertion described by Payne et al. (2017). The semimajor axis of each moon relative to the planet is chosen randomly in the range $r_{\rm min} < a_{\rm moon}/R_H < 0.4$, where $R_{\rm H}$ is the instantaneous Hill radius of the planet at the moment of the first orbit crossing. We considered two $r_{\rm min}$ values of 0.004 and 0.04. This range results in numerically manageable, stable orbits. Payne et al. (2017) found that once moons are liberated from their host planet, the initial conditions of the moons cease to matter due to the intense scattering each moon experiences. The initial inclination of each moon is randomly chosen to be within 1° of the plane of planetary orbits, the eccentricity is set to zero, and all other angles are randomly chosen.

For comparison with our initial conditions, Figure 9 shows the distributions of semimajor axes relative to the host planet Hill radii for solar system moons. Data are gathered from the JPL Solar System Dynamics group, and we assume a uniform density of 2 g cm^{-3} for all bodies. The top panel shows the distribution of semimajor axes of moons by planet, and the lower panel shows the masses for the solar system moons. The range in $a_{\rm moon}/R_H$ in our simulations is seen to coincide with the upper third of the values exhibited by solar system moons; semimajor axes of $a/R_{\rm H} = [0.04,\ 0.4]$ includes most of Jupiter's and Saturn's moons, but not the majority of Uranus' or Neptune's moons (Figure 9).

4.4. Accretion Rates of Liberated Moons

Figure 10 shows an example of the results from one simulation. The lower plot shows the instantaneous periapse of each moon, while the upper figures show snapshots of the orbital configurations. In this simulation, the closest approach

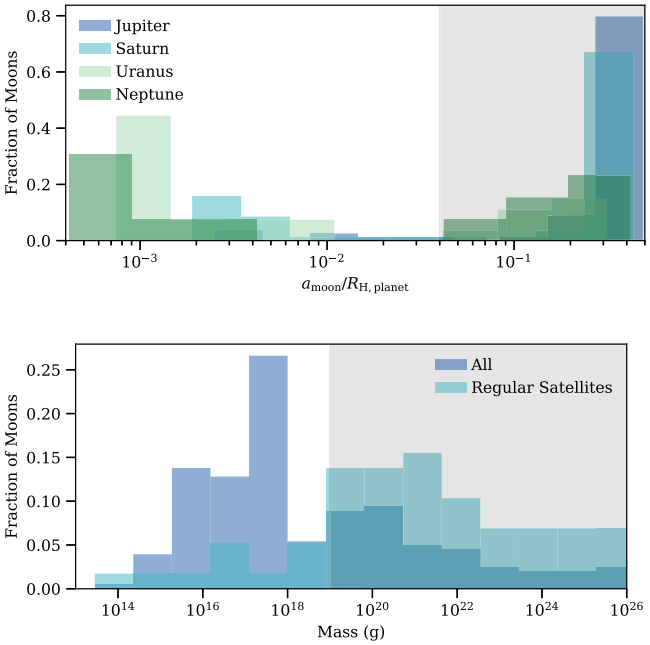

Figure 9. Top: distribution of moon semimajor axes relative to the planet Hill radius, for each of the giant planets. Bottom: distribution of moon masses, including and excluding the irregular satellites. Regular satellites tend to have smaller semimajor axes and larger masses than the irregulars. The shaded portions of each graph show the approximate range of initial semimajor axes that can result in liberated moons (top) and the range of moon masses that can produce observable levels of pollution (bottom), according to our model.

of a moon to the WD is ∼0.007 au. Table 2 lists the closest approaches of each of the moon test particles across all simulations, as well as the initial conditions for each moon's orbit, relative to its host planet.

Of the 60 moons comprising 10 simulations, one enters the Roche limit ($\lesssim$0.005 au) of the WD within the first 200 Myr after WD formation. Additionally, one particle hits a planet, and about half of the moons reach hyperbolic orbits ($e > 1$). We therefore set the accretion rate of liberated moons at 1/60 per 200 Myr after the formation of the host WD. Note that like the asteroid *N*-body results, the moon accretion rates are dependent on the number of bodies available in the system. Our result should be taken as the fraction of liberated moons that accrete. Furthermore, like the asteroid rate, the moon accretion rate is dependent on system architecture and planet masses, and could be much higher in other systems (e.g., Hong et al. 2018).

In our simulations, all moons are liberated from their host planets. Consistent with Payne et al. (2017), as a conservative estimate, we assume that any objects outside of $0.04R_{\rm H}$ of their planet will be liberated. We therefore take the population of solar system moons with semimajor axes in this range as the population of potential moon parent bodies that could pollute a WD. In our solar system, out of a total of about 200 moons, 145 are situated at more than 0.04 $R_{\rm H}$, including the irregular satellites.

Because moon accretions are single events, we can use the J09 accretion model to set a lower limit on the mass of a moon that can provide the minimum observable mass. For the DA of 10,000 K, the least-massive observable parent body is 1.3×10^{19} g, and for the 14,000 K DB, the limit is 1.7×10^{20} g. For the population of solar system moons exterior to our limit for liberation of $0.04R_{\rm H}$, this gives a total of 22 moons that can provide observable pollution on a DA and 10 that can do so on a DB.

We now return to our expression for the frequency of moon accretions, $f_{\rm moons}$ as $N_{\rm moons} \times f_{\rm accrete}$. We found that 1/60 of moons liberated from their host planets are expected to find their way to the WD. Inserting the accretion rate from the *N*-body simulations, and considering the number of moons that can both be accreted and observed on the surface of the WD based on the solar system population of moons, gives $f_{\rm moons,DA} = 22 \times 0.017/200\,{\rm Myr} = 0.0019\,{\rm Myr}^{-1}$ and $f_{\rm moons,DB} = 10 \times 0.017/200\,{\rm Myr} = 0.0009\,{\rm Myr}^{-1}$.

4.5. J09 Model for Moons

Applying the accretion rates of $f_{\rm moons,DA} = 0.0019\,{\rm Myr}^{-1}$ and $f_{\rm moons,DB} = 0.0009\,{\rm Myr}^{-1}$ results in 0.38 and 0.17 accretions in the first 200 Myr past WD formation, for the DA and DB WDs, respectively. One concludes that moons are expected to be visible as single accretion events, with no buildup of pollution from multiple objects, unlike the case for asteroids.

We use solar system moons as a guide for computing the median mass expected for accretion events with moons as parent bodies. In the previous section, we showed that only moons with total masses greater than 1.3×10^{19} g and 1.7×10^{20} g can be detected on the surface of a DA and DB, respectively. In order to obtain the population of observable moons, we therefore select the solar system moons that are above these mass limits, and are situated outside of our assumed liberation limit of $0.04R_{\rm H}$. We assume the resulting moons represent the population of bodies that could both be liberated from their host planets and provide a detectable amount of pollution if they were to be accreted by their host WD. Recall that we found that 22 solar system moons meet these requirements for the DA accretion events and 10 solar system moons for the DB accretion events. Assuming any of these moons would be equally likely to accrete, we used the median mass moon of each population to represent the median mass moon expected to be observed accreting onto each WD type. This results in a median mass for an observed accreted moon on a DA of 1.2×10^{20} g and 3.7×10^{21} g for a DB.

In the lower panels of Figure 8, we show the pollution curve due to accretions of these median mass objects on the same time axis as the asteroid accretions to illustrate how the single events compare with the continuous accretions. We assume that each moon has chondritic composition. Because these are single events, they follow the same phases of accretion as shown in Figure 1; however, we now also show the variation in the abundances of individual elements. The heavy metal limit outlined in Section 3 is shown as a horizontal line in each plot.

For a single moon accretion, the DA case exceeds the mass limit for 0.57 Myr while the DB is observable for 3.89 Myr. Note that these timescales far exceed the duration of observability for a single asteroid on either WD type. However, because asteroid pollution accumulates from multiple bodies, the continuous asteroid calculations result in greater cumulative timescales of observability.

For a mean fraction of observable time for the moons, we multiply these numbers by the expected number of moon accretions in the 200 Myr time period for each case, obtaining $T_{\rm moons,DA} = 0.38$ accretions $\times$ 0.57 Myr/200 Myr $= 0.001$ and $T_{\rm moons,DB} = 0.17$ accretions $\times$ 3.89 Myr/200 Myr $= 0.003$.

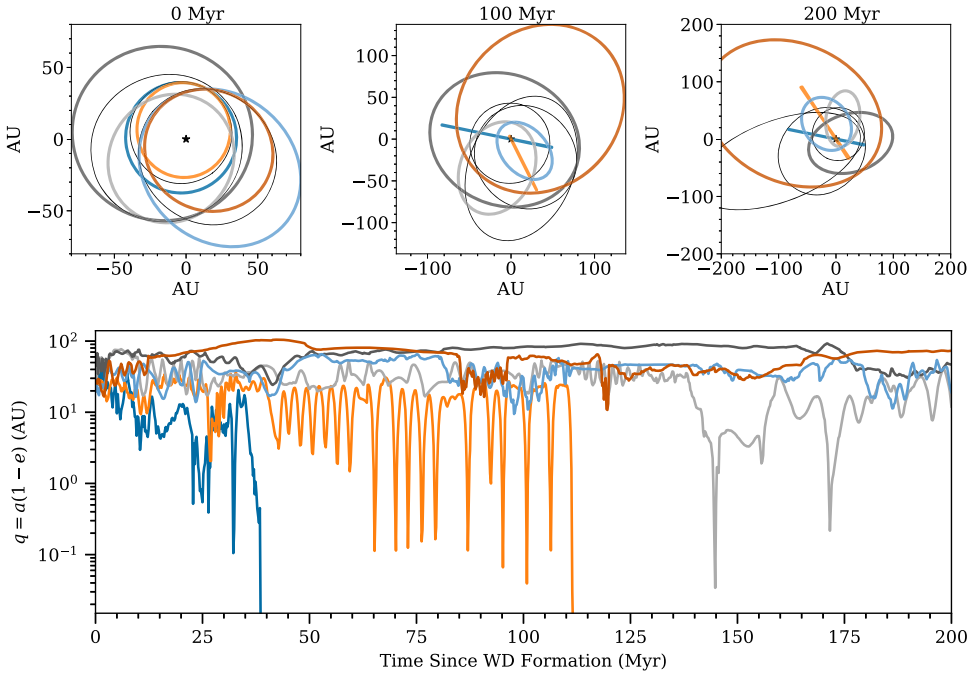

Figure 10. Top: snapshots of orbits from simulation, for planets (thin black lines) and moons (colors). The times indicate the time since the WD formed, and the WD is shown as a black star at 0 au. Bottom: periapse vs. time for the moons, in the same simulation as show in the top plot. Each curve corresponds with the orbits of the same color in the top plot. Two moons are scattered onto hyperbolic orbits following a close approach to the WD.

We can now use our results to evaluate the relative probabilities of detecting asteroids from a debris belt and moons in polluted WDs.

Returning to Equation (1), we now fill in the values derived for the DA and DB cases to find the relative probability of observing accretion of moons and asteroids, yielding

$$\left(\frac{P_{\text{moon accretion}}}{P_{\text{asteroid accretion}}}\right)_{\text{DA}} = \frac{0.001}{0.145} = 0.007 \tag{6}$$

and

$$\left(\frac{P_{\text{moon accretion}}}{P_{\text{asteroid accretion}}}\right)_{\text{DB}} = \frac{0.003}{0.360} = 0.008. \tag{7}$$

Therefore, for three-planet super-Earth/Neptune systems with both moons and asteroids available for accretion, we would only expect up to 1% of polluted DAs and DBs to currently have observable amounts of pollution due to moon accretion.

5. Discussion

Over 1000 WDs have observations of at least one polluting element in the atmosphere (Coutu et al. 2019). Around 20 are considered strongly polluted, with multiple rock-forming elements detected. Therefore, ∼2% of all polluted WDs can be considered "highly polluted." The large, moon-like mass solutions calculated in Section 2 represent the parent bodies associated with this highly polluted sample. Assuming that all of these high-mass parent bodies are indeed moons, this suggests that ∼2% of polluted WDs are accreting moons. Of course, as shown by the pollution masses in Figure 8, accretion of the most-massive asteroids may also result in high masses of pollution, so the population of the most highly polluted WDs may also include the most-massive debris belt members. Nonetheless, this statistic is consistent with our results derived from *N*-body accretion rates, that ∼1% of overall pollution is expected to come from moons as opposed to less-massive debris belt objects.

Uncertainties in this study include the timescales assumed in the J09 model, observational constraints beyond what has been considered in our minimum detectable mass method, exoplanetary moon and asteroid populations, and the effects of planetary architectures beyond the three-planet system considered as our test case. We now explore these various possibilities and their effects on the parent body solutions or numerical accretion models.

5.1. Disk e-folding Timescale

The e-folding lifetime of the debris disks around the WDs, τ_{disk}, determines how quickly pollution accretes onto the WD and, in conjunction with the settling times, limits the maximum mass of any given element that can accumulate in the WD atmosphere (Figure 2). Throughout the asteroid and moon comparison in this paper, we assume $\tau_{\text{disk}} = 10^5$ yr, as an accommodation for estimates that span from 10^4 to 10^6 yr.

In Section 2 we derived t_{min}, the assumed elapsed accretion time that recovers a minimum solution for the parent body mass, or equivalently the steady-state point in the J09 model. Plugging in t_{min} to the J09 model, we can therefore write the general solution for the minimum parent body mass solution relative to the observed mass in the atmosphere as a function of the ratio of the disk and settling timescales, for an arbitrary element:

$$\frac{M_{\text{PB}}(Z, t_{\text{min}})}{M_{\text{CV}}(Z)} = \frac{\frac{\tau_{\text{disk}}}{\tau_{\text{set}}} - 1}{\left(\frac{\tau_{\text{disk}}}{\tau_{\text{set}}}\right)^{\frac{1}{1-\tau_{\text{disk}}/\tau_{\text{set}}}} - \left(\frac{\tau_{\text{disk}}}{\tau_{\text{set}}}\right)^{\frac{1}{\tau_{\text{set}}/\tau_{\text{disk}}-1}}}, \tag{8}$$

where $M_{\text{PB}}(Z, t_{\text{min}})$ is the parent body solution assuming steady state for the element Z, and $M_{\text{CV}}(Z)$ is the observed mass of the

Table 2
Minimum Periapse (q) Reached by Each Moon, in Astronomical Units, and the Parameters Used to Initialize the Moon Orbits

Run	$a_{\rm moon}/R_{\rm H}$ Range	$q1_{\rm min}$ (au)	$q2_{\rm min}$	$q3_{\rm min}$	$q4_{\rm min}$	$q5_{\rm min}$	$q6_{\rm min}$
1	0.004-0.4	0.0612	0.0148	0.0060	20.1982	0.0018	0.0568
2	0.04-0.4	0.6077	4.7049	0.0619	6.6298	7.5362	2.4578
3	0.004-0.4	0.2180	0.1425	0.4133	1.5700	0.0328	0.8134
4	0.004-0.4	0.0078	0.0081	7.9765	0.6881	0.0187	0.0066
5	0.004-0.4	0.9560	1.8188	0.8765	0.0097	3.7238	0.0070
6	0.04-0.4	23.2735	22.1167	15.3154	4.8946	18.0538	17.4935
7	0.04-0.4	19.7743	33.2792	28.4050	19.1263	7.7563	31.6862
8	0.04-0.4	15.2427	11.6404	8.7045	20.0703	7.2406	26.1100
9	0.04-0.4	0.0069	0.0071	0.0341	24.2026	9.4522	10.7774
10	0.04-0.4	8.4775	21.0213	8.5416	0.0065	44.6118	27.5651

Note. $a_{\rm moon}$ is given relative to the Hill radius of the planet. Two moons were inserted around each planet. The WD Roche limit is at 0.005 au.

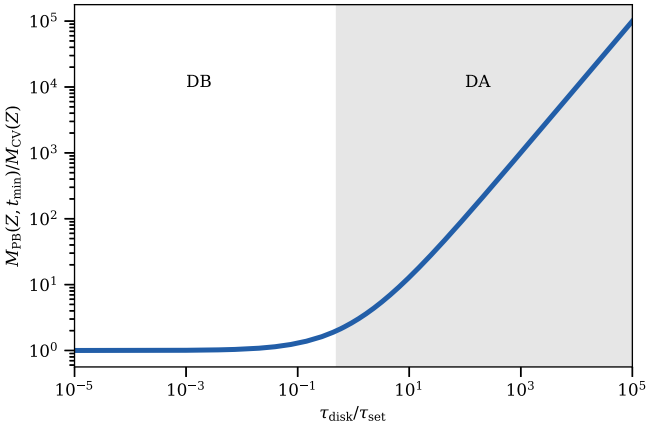

Figure 11. Minimum parent body mass solution relative to the observed mass of pollution in the atmosphere, as a function of the ratio of the disk timescale to the settling time. DAs would be found toward the right, so that the steady-state parent body mass is several times the observed mass in the atmosphere. DBs would be toward the left, where the parent body solution approaches the mass of the polluting metals.

heavy metal. Figure 11 shows Equation (8) applied to a range of disk-to-settling time ratios.

Writing the parent body mass expression in terms of the ratio of characteristic timescales shows why DAs and DBs have different sensitivities to changes in $\tau_{\rm disk}$ (outlined in Section 2) by illustrating the two limits of the parent body mass calculation. If disk timescales far exceed settling times, as they would for DAs, the minimum parent body solution will increase rapidly. For $\tau_{\rm disk} = 10^5$ yr and a DA settling time of days, parent body solutions can reach factors of 10^7 times the observed metal mass. On the other hand, if settling times exceed disk timescales, as they may for DBs, $\tau_{\rm disk}/\tau_{\rm set}$ approaches 1, so that the minimum parent body mass is equal to the current mass of metal in the WD atmosphere.

Increasing the assumed disk timescale would shift parent body mass solutions to the right in Figure 11. While DB WDs with very long settling times would not be strongly affected (parent body solutions would still be roughly equivalent to the mass of metal in the atmosphere), minimum parent body solutions trend approximately linearly with $\tau_{\rm disk}/\tau_{\rm set}$ when the disk timescale exceeds the settling time (DAs). Decreasing the assumed disk timescale would similarly not strongly affect the DBs but would decrease the parent body solutions of the DAs proportionally. Note that WDs with settling times within the range of disk timescale estimates will have nonlinear dependencies on disk timescale. These effects can be seen in the parent body solutions calculated for the observed WDs (Figure 5).

We now return to our parameters $T_{\rm moons}$ and $T_{\rm asteroids}$, the timescales during which pollution exceeds detectable levels. For simplicity, we start by considering a single accretion with a generic observability timescale T. For a single event, T depends on the peak mass of pollution ($M_{\rm CV}$) that can build up in the atmosphere, the duration for which a high mass of pollution can be sustained, and the detection limit associated with the WD.

The maximum mass of pollution deposited by a given parent body mass is the inverse of Equation (8). Therefore, pollution accumulation for DAs varies inversely with changing disk timescales, while peak masses of pollution in DBs remain roughly constant. The amount of time that relatively large masses of pollution can be sustained in the WD atmosphere can be approximated as the difference between $\tau_{\rm disk}$ and $\tau_{\rm set}$. As seen in Figure 4, these timescales are on either side of $t_{\rm min}$, where the maximum $M_{\rm CV}$ is reached. For simplicity, we will consider DA settling times well below, and DB settling times well above, the range of possible disk timescales, so that $|\tau_{\rm disk} - \tau_{\rm set}|$ will be approximately equal to the longest of the two timescales.

Based on this approximation, for DBs $|\tau_{\rm disk} - \tau_{\rm set}| \sim \tau_{\rm set}$, and to a reasonable approximation, changing $\tau_{\rm disk}$ should not affect T for the DBs. Therefore, we anticipate $T_{\rm moons}$ and $T_{\rm asteroids}$ to be robust against disk timescales for DBs of sufficiently long settling times.

DA settling times are short, so $|\tau_{\rm disk} - \tau_{\rm set}| \sim \tau_{\rm disk}$, and increasing the disk timescale will lengthen the amount of time that peak pollution levels can be sustained. However, increasing $\tau_{\rm disk}$ decreases the maximum mass of pollution that can be accumulated. If the decreased pollution masses still exceed the detection limit, then T would increase, but if the new pollution masses do not exceed detection limits, T would fall to zero. The overall effect on $T_{\rm moons}$ and $T_{\rm asteroids}$ will therefore depend on the detection limits and distribution of debris belt masses considered. For our distributions of moons and asteroids, generally only the most-massive bodies are contributing toward observable pollution, so assuming that most pollution would remain above the detection threshold, we would expect $T_{\rm moons}$ and $T_{\rm asteroids}$ to increase with increases in disk timescale.

5.2. Asteroid Belt Mass and Size Distribution

The accretion rate extrapolated from *N*-body simulations depends on the number of objects in the asteroid belt, which in turn depends on the total mass and assumed distribution of radii for the population of asteroids. Furthermore, the number of bodies contributing to heavy element pollution at any given time, and therefore the median mass of heavy elements in the WD convection zone, varies directly with the accretion rate. In this work, we assumed a solar system mass asteroid belt, with radii spanning 0.5–500 km following a distribution of $dN \propto r^{-3.5}dr$.

Due to the continuous nature of asteroid accretion, pollution remains at a relatively stable minimum for the duration of accretion ($\sim 10^{16}$ g total in the DA, $\sim 10^{20}$ g for the DB), with short spikes to greater, observable masses when a particularly massive asteroid accretes. Whether asteroid accretion is observable for long time periods is therefore an "all or nothing" issue, and is very sensitive to how a typical amount of accumulated heavy elements compares to the detection limit. If the limit is just above the typical mass that can build up from multiple accretions, we will observe only the peaks of the most-massive asteroid accretions. However, if the detectability limit is just below the typical mass of accumulated metals, accretion is observable for the entire time period.

Given that many polluted WD progenitors are estimated to be more massive than the Sun (Coutu et al. 2019), it is reasonable to assume that many of these systems may have had debris belts more massive than the asteroid belt. If the debris in these more-massive belts follows the same collisionally produced power-law distribution as described for the asteroid belt, there would be correspondingly more objects of any given mass. Assuming the accretion rates per number of available bodies is unchanged, a larger debris belt would increase the total number of accretion events, and therefore increase the typical pollution mass at every point in time, resulting in a larger $T_{\rm asteroids}$. If the moon accretions remain unchanged, this increase in $T_{\rm asteroids}$ would decrease the fraction of pollution that would be due to moons.

Finally, we consider that the overall distribution of debris belts may be truncated during post-main-sequence stellar evolution. Veras et al. (2014) and Veras & Scheeres (2020) found that bodies less than about 10 km in radius can be disrupted by the YORP effect and subsequently ground down, effectively removing bodies of 10^{19} g and smaller from the asteroid population. The pollution curve resulting from the J09 model for semicontinuous accretion can be thought of as two components: the steady background pollution caused by the accretion of many small bodies, and the larger peaks generated by massive asteroids. For the system examined in this work, we find that the background is orders of magnitude lower than the most-massive peaks of pollution. All else equal, eliminating the small end of the asteroid distribution therefore reduces the level of background pollution, preventing many of the lower-mass accretion events from exceeding the detection threshold, though the peak pollution masses are left unchanged. Applying our model to a truncated debris belt distribution, we find that the truncation has a stronger effect for the DB case, where $T_{\rm asteroids}$ is reduced by about half. For the DA, $T_{\rm asteroids}$ remains unchanged, likely because the quick settling time reduces the amount of background material that could build up in the original case.

5.3. Debris Belt Accretion Mechanisms

In this work we have focused on the accretion process proposed by Mustill et al. (2018), which relies on planet instabilities following the onset of stellar mass loss. Alternative mechanisms for transporting material to the WD include perturbations from third bodies or secular evolution (Petrovich & Muñoz 2017; O'Connor et al. 2022). These scenarios predict much more efficient accretion of debris belts than Mustill et al. (2018), with up to 70% of the objects in the debris belt being accreted. In this section we explore the effect of these alternative pollution mechanisms and show that while the more efficient mechanisms for pollution would increase the probability of observing asteroids, they also imply an order-of-magnitude greater fraction of highly polluted WDs than is observed. We arrive at this conclusion by comparing the rate of asteroid accretion required to match the observed population of highly polluted WDs to the disk mass accretion rates implied by the models. This analysis suggests that while more efficient mechanisms are possible, Mustill et al. (2018) broadly provide the most consistent baseline accretion rate for asteroids given observational constraints.

To assess the need for alternative pollution mechanisms, we first calculate the accretion rate required by the observed fraction of highly polluted WDs. The highly polluted DBs in our sample, comprising approximately 1% of WDs in general, have at least 10^{22} g of polluting metals each. For this calculation, we consider the DB mass limit to apply to the DAs as well, given uncertainties in the effects of mixing for the DAs. As an upper limit for the required accretion rates, let us assume that all of the observed pollution is due to asteroids, ignoring moons for the moment. Based on the asteroid distribution used throughout this study, we find that this high mass range represents about 2×10^{-6} of the total number of bodies. The probability of observing one of these massive asteroids accreting is equal to the number of massive bodies we expect to accrete in the 200 Myr time period multiplied by the fraction of time that the object is observable in the WD. To first order, the pollution from such a massive object will be observable for the longest characteristic timescale—in other words, the settling timescales for the DBs and the disk timescales for the DAs. All together, this puts a constraint on the fractional accretion rate of $1\% = N_{>10^{22}\rm g} \times \dot{f} \times \tau_{\rm set/disk}$, where $N_{>10^{22}\rm g}$ is the number of bodies greater than 10^{22} g, $\dot{f}$ is the fraction of the belt accreted per million years, and $\tau_{\rm set/disk}$ is the longer of the characteristic timescales for the DBs or DAs, as described above. For a given $N_{>10^{22}\rm g}$ and $\tau_{\rm set/disk}$, we can therefore solve for the fractional accretion rate required to result in a 1% chance of observing a massive body. For a typical DB with $\tau_{\rm set} \sim 1$ Myr, we require $N_{>10^{22}\rm g} \times \dot{f} \sim 0.01\ {\rm Myr}^{-1}$. For the debris disk mass used in this work, 3×10^{24} g, we find 10^7 objects total in the debris belt, around 24 of which are above the mass cutoff of 10^{22} g. This gives a fractional accretion rate for the DBs of $\dot{f} = 4 \times 10^{-4}\ {\rm Myr}^{-1}$, within a factor of four of the Mustill result. For the DAs, using $\tau_{\rm disk} \sim 10^5$ yr, we find $\dot{f} = 4 \times 10^{-5}\ {\rm Myr}^{-1}$, and we consider this a lower limit, as it is possible to detect somewhat lower masses of pollution on DAs.

While the O'Connor et al. (2022) and Petrovich & Muñoz (2017) studies do not use *N*-body simulations, and obtaining a fractional rate is not as straightforward, both studies reach accretion rates of $10^9\ {\rm g\ s}^{-1}$ with disk masses of approximately

3×10^{24} g and the assumption of steady-state disks. Applying the asteroid distribution used here, we can translate this rate to a fractional accretion rate with respect to total disk mass for comparison to the results of Mustill et al. (2018), yielding $10^9\ \mathrm{g\ s^{-1}}/M_{\mathrm{disk}} \sim 5 \times 10^{-3}\ \mathrm{Myr^{-1}}$. For this fractional accretion rate, we would expect to see heavy pollution for about 10% of WDs instead of the observed 1%.

5.4. The Impact of Planet Spacing on Moon Liberation

Because moon liberations depend on close encounters between planets, and planet separations determine how quickly systems can become unpacked during stellar evolution, we expect the frequency of moon liberations to vary with planetary system architectures. The three-planet system used throughout Section 4 has spacings of five to seven mutual Hill radii, with the innermost planet situated at 10 au. This arrangement of planets is somewhat more tightly packed than most observed systems. Separations for systems detected by the Kepler satellite generally peak around 14–20 mutual Hill radii (Pu & Wu 2015; Weiss et al. 2018); however, these observed planets are all on orbits interior to ∼2 au, and it is unclear if this trend would directly apply to outer planets.

One constraint on outer planet spacings is HR 8799 (Marois et al. 2008, 2010), which hosts four giant planets ($> 5M_{\mathrm{Jup}}$) exterior to 10 au, and is a likely candidate for a future polluted WD system (Veras & Hinkley 2021). Considering the most stable configuration for these planets (Goździewski & Migaszewski 2020), separations are approximately two to three mutual R_{H}. From the sample of directly imaged exoplanets, Nielsen et al. (2019) found that approximately 9% of stars more massive than $1.5M_{\odot}$ could host such massive planets outside of 10 au.

In Figure 12 we show the orbital crossings that result in simulations with initial planet spacings of 5–10, 10–20, and 20–30 mutual Hill radii. Planet masses for all three simulations are 1.3, 30.6, and 7.8 $M_{\oplus}$, the same as used in Section 4. These simulations result in 502, 148, and 173 crossings for the 5–10, 10–20, and 20–30 cases, respectively. We find that while the number of crossings varies with planet spacings, crossings do still occur even at spacings more consistent with the majority of observed systems. From this simple comparison, we do not anticipate that orbital crossings, and consequently moon liberations, would be entirely eliminated for more widely separated systems. Further study is necessary for more detailed connections between liberations and accretions and planetary architectures.

5.5. Populations of Exomoons

In this paper, we assumed that moon populations would be similar to those in the solar system. It is possible that moon populations in exoplanetary systems do not resemble the solar system. However, as there are no confirmed detections of rocky or icy exomoons, it is difficult to determine how many such moons a typical exoplanetary system might have. Additionally, if exomoons in general are not found in all planetary systems, the probabilities of moon accretions derived in this work should be multiplied by the fraction of polluted WD systems that do host exomoons.

A first-order limit on the number of moons in a given WD system should be the placement of moon-hosting planets. Dobos et al. (2021) found that whether exomoons can survive

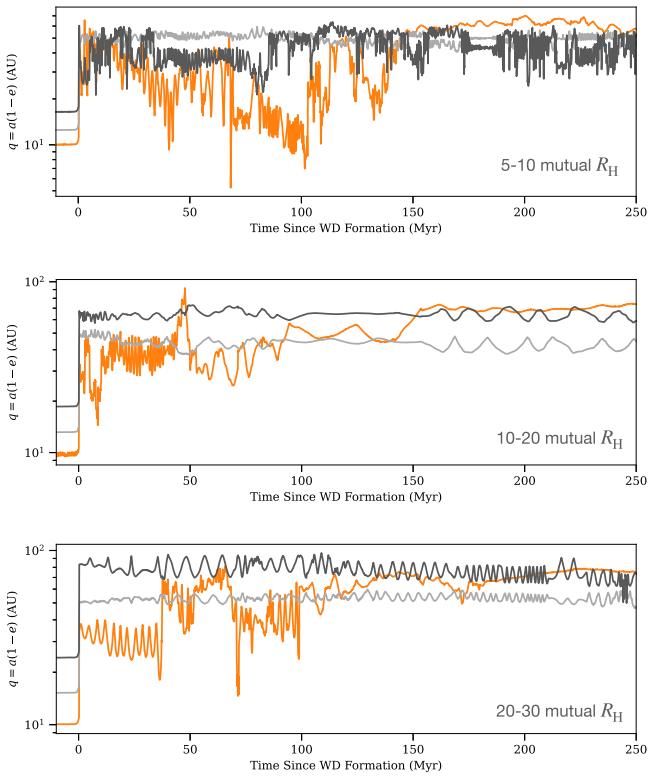

Figure 12. The periapse evolution of three-planet systems for three different ranges of planet spacings in terms of mutual Hill radii: 5–10 (top), 10–20 (middle), and 20–30 (bottom). In each system, the innermost planet is at 10 au and the spacings between each consecutive planet are randomly chosen from the stated ranges. Planet masses for all three simulations are 1.3, 30.6, and 7.8 $M_{\oplus}$. While the most closely packed system experiences the most orbital crossings between planets, crossings still occur in the more widely spaced systems.

in a stable orbit around a given planet depends on the proximity of the planet to the host star. They conclude that planets on very short-period orbits (<100 days) are most limited in the fraction of moons they can retain, while planets with longer periods could retain at least 60% of their original moons. For the purposes of determining the populations of moons available to accrete onto a WD, the longer-period planets are likely more relevant, as the inner planets risk being engulfed by the star in its red giant phase.

In our three-planet system, planets were originally located 10–13 au around a $3M_{\odot}$ star, with periods of 18–27 yr. According to the Dobos et al. (2021) study, these planets could retain about 70% of their moons. The giant planets of the solar system have orbital periods of about 11–160 yr, and have a similar moon retention fraction of 60%–80%. This suggests that whether or not the distributions in mass and semimajor axis of moons in our theoretical three-planet system match those for our solar system's moons, systems resembling our three-planet system should have a large portion of their moons intact and bound to planets when the WD forms. Further constraints on exomoon populations could be made as transit timing variation searches for exomoon progress (e.g., Kipping 2021; Teachey & Kipping 2021).

6. Conclusions

Motivated by the large parent body masses required to explain observed levels of WD pollution, and the recent

discovery of beryllium in a WD atmosphere, we have used *N*-body simulations and the Jura et al. (2009) accretion model to assess the likelihood that a WD will be polluted by a moon. We focus this study on the first 200 Myr past WD formation for a planetary system containing three super-Earth/Neptune-class planets. Extrapolating from asteroid *N*-body simulations, we find that such a planetary system could sustain an asteroid accretion rate of approximately 1200 objects per million years. Assuming that the system had a population of moons similar to the regular solar system moons, we find from *N*-body simulations that we could expect up to about 0.4 moon accretions per 200 Myr.

Using the population of observed WDs with calcium detections, we find that the pollution must have a calcium mass component of at least 5.8×10^{14} g to be observable in a DA atmosphere, and 1.4×10^{18} g to be detected in a DB. We use these limits to determine the cumulative fractions of time that moons and asteroids can produce observable levels of pollution. Based on our numerical accretion model, we expect $\sim$1% of WD pollution to come from moons as opposed to asteroids. If we consider, as a first-order approximation, that all of the most highly polluted WDs (requiring the most-massive parent bodies) are polluted by moons, our parent body mass approach returns a similar statistic, of moons making up about 2% of polluters.

C.M. and K.J.W. acknowledge support from NSF grants SPG-1826583 and SPG-1823617. E.D.Y. acknowledges support from NASA Exoplanets grant 80NSSC20K0270.

ORCID iDs

Isabella L. Trierweiler https://orcid.org/0000-0002-4872-1021
Alexandra E. Doyle https://orcid.org/0000-0003-0053-3854
Carl Melis https://orcid.org/0000-0001-9834-7579
Kevin J. Walsh https://orcid.org/0000-0002-0906-1761

References

Bauer, E. B., & Bildsten, L. 2018, ApJL, 859, L19
Bauer, E. B., & Bildsten, L. 2019, ApJ, 872, 96
Blouin, S., Dufour, P., & Allard, N. F. 2018, ApJ, 863, 184
Coutu, S., Dufour, P., Bergeron, P., et al. 2019, ApJ, 885, 74
Debes, J. H., & Sigurdsson, S. 2002, ApJ, 572, 556
Dobos, V., Charnoz, S., Pál, A., Roque-Bernard, A., & Szabó, G. M. 2021, PASP, 133, 094401
Dohnanyi, J. S. 1969, JGR, 74, 2531
Doyle, A. E., Desch, S. J., & Young, E. D. 2021, ApJL, 907, L35
Doyle, A. E., Klein, B., Schlichting, H. E., & Young, E. D. 2020, ApJ, 901, 10
Dufour, P., Blouin, S., Coutu, S., et al. 2017, in ASP Conf. Ser. 509, 20th European White Dwarf Workshop, ed. P. E. Tremblay, B. Gaensicke, & T. Marsh (San Francisco, CA: ASP), 3
Dufour, P., Kilic, M., Fontaine, G., et al. 2012, ApJ, 749, 6
Farihi, J., Gänsicke, B. T., & Koester, D. 2013, Sci, 342, 218
Farihi, J., Koester, D., Zuckerman, B., et al. 2016, MNRAS, 463, 3186
Fortin-Archambault, M., Dufour, P., & Xu, S. 2020, ApJ, 888, 47
Gänsicke, B. T., Koester, D., Farihi, J., et al. 2012, MNRAS, 424, 333
Giorgini, J. D., Yeomans, D. K., Chamberlin, A. B., et al. 1996, AAS/Division for Planetary Sciences Meeting Abstracts, 28, 25.04
Girven, J., Brinkworth, C. S., Farihi, J., et al. 2012, ApJ, 749, 154
Goździewski, K., & Migaszewski, C. 2020, ApJL, 902, L40
Hong, Y.-C., Raymond, S. N., Nicholson, P. D., & Lunine, J. I. 2018, ApJ, 852, 85
Hoskin, M. J., Toloza, O., Gänsicke, B. T., et al. 2020, MNRAS, 499, 171
Hurley, J. R., Pols, O. R., & Tout, C. A. 2000, MNRAS, 315, 543
Jura, M. 2003, ApJL, 584, L91
Jura, M., Muno, M. P., Farihi, J., & Zuckerman, B. 2009, ApJ, 699, 1473
Jura, M., Xu, S., Klein, B., Koester, D., & Zuckerman, B. 2012, ApJ, 750, 69
Kipping, D. 2021, MNRAS, 507, 4120
Klein, B., Jura, M., Koester, D., & Zuckerman, B. 2011, ApJ, 741, 64
Klein, B. L., Doyle, A. E., Zuckerman, B., et al. 2021, ApJ, 914, 61
Koester, D. 2009, A&A, 498, 517
Koester, D., Gänsicke, B. T., & Farihi, J. 2014, A&A, 566, A34
Koester, D., Kepler, S. O., & Irwin, A. W. 2020, A&A, 635, A103
Koester, D., Rollenhagen, K., Napiwotzki, R., et al. 2005, A&A, 432, 1025
Maldonado, R. F., Villaver, E., Mustill, A. J., & Chávez, M. 2022, MNRAS, 512, 104
Marois, C., Macintosh, B., Barman, T., et al. 2008, Sci, 322, 1348
Marois, C., Zuckerman, B., Konopacky, Q. M., Macintosh, B., & Barman, T. 2010, Natur, 468, 1080
Melis, C. 2016, in IAU Symp. 314, Young Stars & Planets Near the Sun, ed. J. H. Kastner, B. Stelzer, & S. A. Metchev (Cambridge: Cambridge Univ. Press), 241
Melis, C., & Dufour, P. 2017, ApJ, 834, 1
Mustill, A. J., Villaver, E., Veras, D., Gänsicke, B. T., & Bonsor, A. 2018, MNRAS, 476, 3939
Nielsen, E. L., De Rosa, R. J., Macintosh, B., et al. 2019, AJ, 158, 13
O'Connor, C. E., Teyssandier, J., & Lai, D. 2022, MNRAS, 513, 4178
Payne, M. J., Veras, D., Gänsicke, B. T., & Holman, M. J. 2017, MNRAS, 464, 2557
Payne, M. J., Veras, D., Holman, M. J., & Gänsicke, B. T. 2016, MNRAS, 457, 217
Petrovich, C., & Muñoz, D. J. 2017, ApJ, 834, 116
Pu, B., & Wu, Y. 2015, ApJ, 807, 44
Rein, H., & Liu, S. F. 2012, A&A, 537, A128
Rein, H., & Spiegel, D. S. 2015, MNRAS, 446, 1424
Stephan, A. P., Naoz, S., & Zuckerman, B. 2017, ApJL, 844, L16
Swan, A., Farihi, J., Koester, D., et al. 2019, MNRAS, 490, 202
Teachey, A., & Kipping, D. 2021, MNRAS, 508, 2620
Veras, D., & Gänsicke, B. T. 2015, MNRAS, 447, 1049
Veras, D., & Hinkley, S. 2021, MNRAS, 505, 1557
Veras, D., Jacobson, S. A., & Gänsicke, B. T. 2014, MNRAS, 445, 2794
Veras, D., Mustill, A. J., Gänsicke, B. T., et al. 2016, MNRAS, 458, 3942
Veras, D., & Scheeres, D. J. 2020, MNRAS, 492, 2437
Weiss, L. M., Marcy, G. W., Petigura, E. A., et al. 2018, AJ, 155, 48
Wilson, D. J., Gänsicke, B. T., Koester, D., et al. 2015, MNRAS, 451, 3237
Xu, S., Dufour, P., Klein, B., et al. 2019, AJ, 158, 242
Xu, S., Jura, M., Klein, B., Koester, D., & Zuckerman, B. 2013, ApJ, 766, 132
Xu, S., Jura, M., Koester, D., Klein, B., & Zuckerman, B. 2014, ApJ, 783, 79
Xu, S., Zuckerman, B., Dufour, P., et al. 2017, ApJL, 836, L7
Zhang, Y., Liu, S.-F., & Lin, D. N. C. 2021, ApJ, 915, 91
Zuckerman, B., Koester, D., Dufour, P., et al. 2011, ApJ, 739, 101
Zuckerman, B., Melis, C., Klein, B., Koester, D., & Jura, M. 2010, ApJ, 722, 725